(article starts on next page)

Evolution of microstructure and mechanical properties during annealing of heavily rolled AlCoCrFeNi$_{2.1}$ eutectic high-entropy alloy

Adrianna Lozinko [a,1], Reza Gholizadeh [b,1], Yubin Zhang [c], Uta Klement [a], Nobuhiro Tsuji [b,d], Oleg V. Mishin [c,*], Sheng Guo [a,**]

[a] *Department of Industrial and Materials Science, Chalmers University of Technology, SE-41296, Gothenburg, Sweden*
[b] *Department of Materials Science and Engineering, Kyoto University, Sakyo-ku, Kyoto, 606-8501, Japan*
[c] *Department of Mechanical Engineering, Technical University of Denmark, DK-2800 Kgs. Lyngby, Denmark*
[d] *Elements Strategy Initiative for Structural Materials (ESISM), Kyoto University, Sakyo-ku, Kyoto, 606-8501, Japan*

ARTICLE INFO

ABSTRACT

Changes in the microstructure and mechanical properties during annealing at 800 °C have been characterized in a 90% cold-rolled AlCoCrFeNi$_{2.1}$ eutectic high-entropy alloy containing the FCC and B2 (ordered BCC) phases. In the as-rolled condition, the FCC phase is found to contain a high frequency of finely spaced deformation-induced boundaries, which provides a high driving force for recrystallization within this phase. Quantitative analysis of electron backscatter diffraction data from the annealed samples indicates that recrystallization progresses faster in the FCC phase than in B2 regions. Although recrystallization leads to substantial coarsening of the microstructure, the average recrystallized grain size remains in the submicron range even after 2 h at 800 °C. Tensile test data demonstrate that combinations of high yield strength and good ductility are obtained in partially recrystallized samples produced by annealing for 2.5–10 min. However, the work-hardening capacity of each annealed sample is lower than that of the cold-rolled sample. Furthermore, for the samples annealed for at least 5 min a yield drop is observed soon after the onset of plastic deformation. Analysis of the microstructure and mechanical behavior in several annealed AlCoCrFeNi$_{2.1}$ samples indicates a clear correlation between the magnitude of the yield drop and the recrystallized fraction. The mechanical behavior of the AlCoCrFeNi$_{2.1}$ alloy studied in this work is compared with that reported in previous publications.

1. Introduction

High-entropy alloys (HEAs) defined as alloys containing at least five principal elements have attracted significant attention due to interesting combinations of physical and mechanical properties [1–5]. Studies of HEAs initially focused on as-cast single-phase alloys, for many of which it appeared difficult to reach a good balance of strength and ductility, as desired for industrial applications. Therefore, research has broadened to multiphase HEAs to explore precipitation strengthening [6–11], transformation-induced plasticity (TRIP) [12–17] and eutectic/eutectoid systems [18–20]. In particular, a combination of a comparatively high strength and high ductility was observed in ingots of an AlCoCrFeNi$_{2.1}$ eutectic high-entropy alloy (EHEA) [20–23]. This combination is enabled by alternating FCC(L1$_2$) and BCC(B2) lamellae, where the soft FCC(L1$_2$) phase provides high ductility, while the hard BCC(B2) phase increases the overall strength. Phase boundaries hinder dislocation motion and thus also contribute to the mechanical strength of the ingots [22].

Attempts to further improve mechanical properties of the as-cast AlCoCrFeNi$_{2.1}$ alloy were made using either warm, cold or cryo-rolling with subsequent annealing. It was shown that heavy rolling at 750 °C, as well as recrystallization annealing of heavily cold- or cryo-rolled samples, resulted in improved combinations of strength and ductility in this alloy [24–28]. As these annealing experiments involved only isochronal (1 h) annealing at different temperatures, the recrystallization kinetics were not considered in Refs. [24–28]. Furthermore, the evolution of mechanical properties during the course of static recrystallization was not analyzed in these previous reports.

Therefore, the goal of the present work is to quantify the progress of recrystallization in heavily rolled AlCoCrFeNi$_{2.1}$ and to relate microstructural changes during this process to the evolution of strength and ductility. Samples of heavily rolled AlCoCrFeNi$_{2.1}$ are investigated in this work after annealing at 800 °C for different periods of time. Microstructural information obtained using transmission electron microscopy (TEM), scanning electron microscopy (SEM) and backscatter electron diffraction (EBSD) is used to discuss the evolution of mechanical properties assessed through tensile tests. Finally, mechanical properties measured in this study are compared with those reported for AlCoCrFeNi$_{2.1}$ in other conditions.

2. Experimental

The AlCoCrFeNi$_{2.1}$ alloy (elements in atomic ratios) was prepared by arc melting of high purity (>99.9%) metal billets in a Ti-gettered argon atmosphere, and the obtained material was re-melted four times to achieve good macroscopic homogeneity. The alloy was finally drop cast into $10 \times 10 \times 60 \ mm^3$ ingots. These ingots were thicker than those used in Refs. [24–27], which resulted in a slower cooling rate and in a different as-cast microstructure compared to that in the ingots used in the previous studies. For example, the lamella widths (thicknesses) measured in our ingots [29] were larger than those reported in Refs. [24–27].

The obtained ingots were cold rolled by multiple passes to a total reduction in thickness of 90%. To avoid significant heterogeneities caused by roll-gap geometry, the l/h ratio, where l is the chordal length of the contact between the rolls and the sample, and h is the mean sample thickness [30,31], was maintained within the range 2–3. Side edges of the samples were ground after 20% and 75% rolling to prevent extensive edge cracking. The cold-rolled material was heated to 800 °C within ~10 s and then annealed at this temperature in argon atmosphere for different periods of time in the range from 2.5 min to 2 h, followed by cooling in air.

The microstructure in each sample was studied in the longitudinal section containing the rolling direction (RD) and the normal direction (ND). The samples were investigated in different laboratories using several field emission gun scanning electron microscopes, Zeiss Leo 1550, Zeiss Gemini II 450, JSM-7000F and JSM-7800F. The as-deformed condition and the sample annealed for 2.5 min were additionally studied by TEM using JEOL 2100 and FEI Tecnai T20 microscopes. Thin foils for the TEM analysis were prepared by twin jet electropolishing. Specimens for SEM/EBSD were produced by mechanical polishing, applying a Struers OP-S suspension in the final polishing step. For each sample, backscattered electron (BSE) images were taken to observe the microstructure at different magnifications. EBSD data were then acquired using the AZtec system from Oxford Instruments, measuring crystallographic orientations with a step size of either 20 nm or 40 nm, and covering several regions with a total area of ~20000 μm^2 for each sample. During the EBSD analysis, crystallographic parameters of FCC iron and BCC iron were applied as match units for indexing diffraction patterns from FCC and B2 regions, respectively.

The collected EBSD data were post-processed using the Channel 5 software. In these data, low angle boundaries (LABs) and high angle boundaries (HABs) were defined as boundaries with misorientation angles $\theta = 2–15°$ and $\theta > 15°$, respectively. Adjacent pixel misorientations <2° were ignored because of the limited angular resolution of the EBSD technique. Recrystallized grains were defined as regions with grain orientation spread (GOS) below 1° and an equivalent circular diameter of at least 0.2 μm. This minimum size was chosen based on TEM and SEM observations of the microstructure, where recrystallized FCC grains containing annealing twins were at least ~0.2 μm large. Note that annealing twins were treated as individual crystallites when calculating the GOS, while grain sizes within low-GOS subsets were measured ignoring twin boundaries. Fractions of different texture components were calculated within 15° from their exact orientations.

Tensile test specimens with a gauge length of 5 mm, width of 1.2 mm and the tensile axis along the RD were cut using a Brother HS-70A wire electric discharge machine. Prior to tensile testing, the initial specimen thickness was reduced to 0.6 mm by mechanical polishing of both sides of each specimen, and randomly distributed speckle patterns were then sprayed on the specimen surface to enable digital image correlation (DIC) measurements. For each condition, three specimens were deformed at room temperature using a Shimadzu AG-100kNXplus tensile testing machine at an initial strain rate of $8.3 \times 10^{-4} \ s^{-1}$. DIC images were recorded using a CCD camera at a speed of 5 frames/s and analyzed using the Vic-2D software.

3. Results

3.1. Microstructure

It has been previously shown that the FCC(L1$_2$) phase present in the as-cast microstructure of AlCoCrFeNi$_{2.1}$ undergoes disordering during heavy rolling, while the ordered B2 phase is retained even after 90% rolling [25]. The heavily rolled material is thus comprised of FCC and B2 regions, which can be distinguished in BSE images due to atomic number contrast, with B2 regions appearing darker than the FCC phase (see Fig. 1a). The deformed microstructure predominantly consists of fine lamellar structures with alternating FCC and B2 lamellae, although in some areas the B2 phase is observed in the form of short and rather thick fragments of coarse B2 structures. Microshear bands at 20°–35° to the RD are also observed in multiple locations. TEM reveals significant differences in the boundary spacing for the two phases (Fig. 1b). The average boundary spacing between lamellar boundaries measured along the ND is ~30 nm in the FCC phase, while the average thickness of B2 structures is significantly greater, 130 nm. Dislocation densities appear to be fairly high in each phase.

The microstructure after annealing at 800 °C for 2.5 min is much more heterogeneous than the cold-rolled material. In the annealed microstructure, non-recrystallized areas with high dislocation densities are combined with apparently recrystallized grains of FCC and B2 phases (see Fig. 2 and Fig. 3a). Some non-recrystallized regions contain comparatively coarse and slightly elongated subgrains, while other regions exhibit fine lamellar structures (LS) morphologically similar to those in the as-deformed microstructure. Additionally, arrays of small B2 crystallites are seen within the non-recrystallized regions of the FCC phase. These B2 crystallites can be either remnants of initially fine B2 lamellae, which became discontinuous due to migration of phase boundaries, or precipitates formed during annealing [28,32,33]. A number of B2 particles are also observed within recrystallized FCC regions (see Fig. 3a).

An example phase map collected using EBSD in the sample annealed for 2.5 min and regions identified as recrystallized in this map are presented in Fig. 3b and c. It is evident that most of the recrystallized FCC grains (easily recognizable due to the presence of annealing twins) are successfully detected using the criteria described in Section 2. Therefore, the applied approach is considered appropriate also for detecting recrystallized B2 grains. Analysis of the EBSD data obtained from several large areas of this sample suggests that the microstructure is 63% recrystallized. Considering recrystallized fractions in each phase separately, the area fraction of recrystallized grains f_{Rex} within the FCC phase is larger, 68%, than within B2 regions, 55%. The average size of recrystallized grains in this condition is 320 nm for the FCC phase and ~300 nm for the B2 phase.

More extended annealing at 800 °C leads to a larger recrystallized grain size and a greater recrystallized area fraction (Fig. 4). The overall f_{Rex} is 71% after annealing for 5 min and 84% after annealing for 10 min. In the sample annealed for 30 min, recrystallization is almost complete within the FCC phase ($f_{Rex} = 95\%$), while f_{Rex} is only 80% in the B2 regions. The non-recrystallized B2 regions in this sample are represented both by clusters of several subgrains having very low misorientations
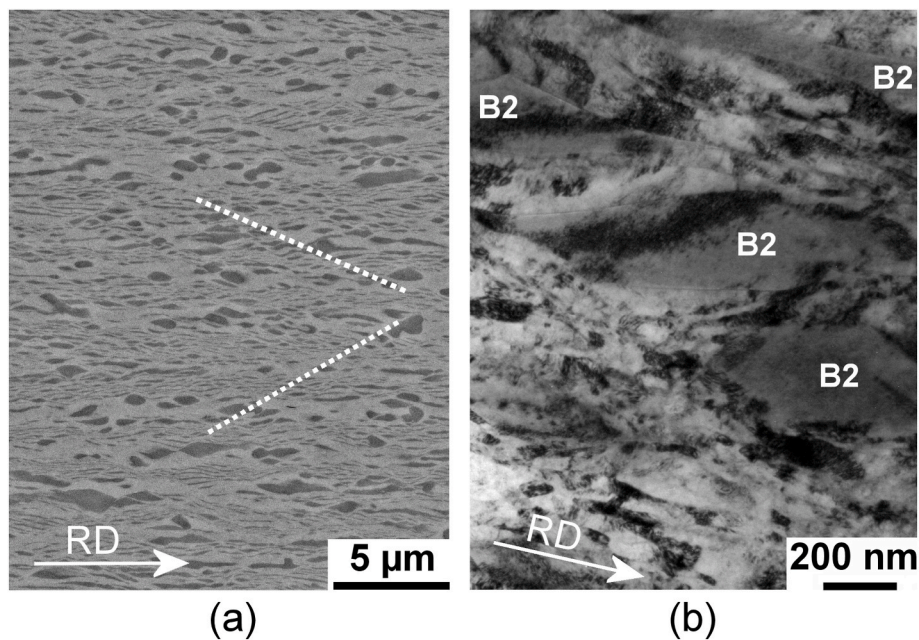
Fig. 1. Microstructure of the cold-rolled sample: (a) BSE image where light and darker regions correspond to FCC and B2 phases, respectively. The dashed lines indicate examples of microshear bands; (b) TEM image showing the deformed microstructure in more detail. In this image, fine FCC lamellar structures are combined with coarser B2 structures.
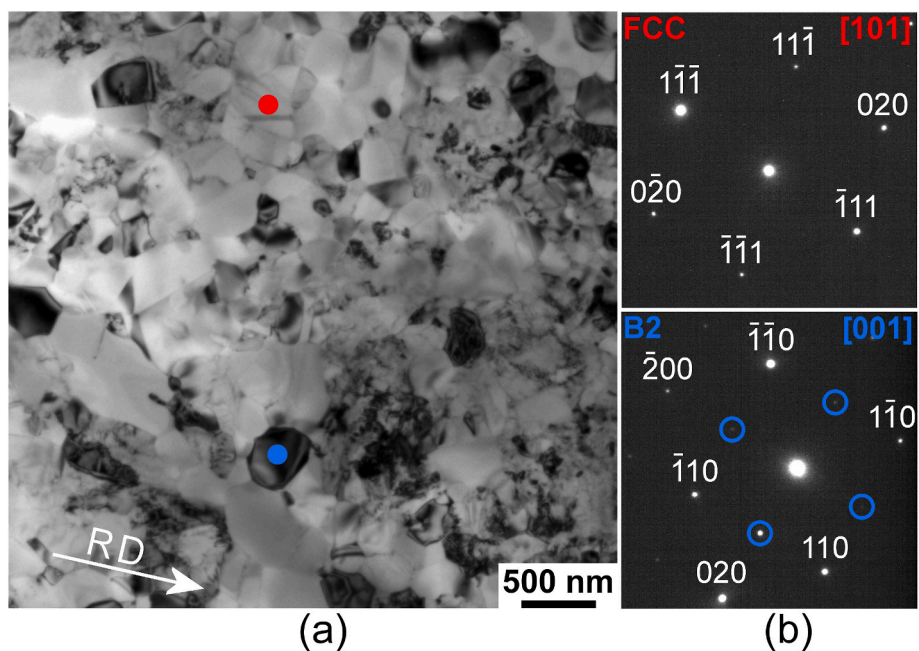

Fig. 2. Bright-field TEM image (a) and selected area diffraction (SAD) patterns (b) from the sample annealed for 2.5 min at 800 °C. Red and blue circles in (a) indicate the crystallites from which the SAD patterns were obtained. Encircled spots in (b) are superlattice reflections. Numbers in brackets correspond to indices of zone axes. (For interpretation of the references to colour in this figure legend, the reader is referred to the Web version of this article.)

and by isolated particles with a size of <0.2 μm, such as those seen in Fig. 5. The microstructure is almost fully recrystallized after annealing for 1 h and 2 h, although f_{Rex} in the B2 regions is still considerably lower than that in the FCC phase (see Fig. 6a).

Fig. 6b shows that as the annealing duration increases, recrystallized FCC grains become significantly coarser than B2 grains. The average recrystallized grain sizes d_{Rex} in the sample annealed for 2 h are 450 nm and 530 nm in the B2 and FCC regions, respectively (Fig. 6b), and ~500 nm when averaged over all grains. The directionality of this

microstructure is less pronounced compared to that after short annealing treatments (see Figs. 3 and 4).

Despite the substantial microstructural changes taking place during material processing, the proportion of the different phases is only slightly different from that in the as-cast condition. Assuming that the fraction of the B2 phase measured in the as-cast condition is not affected by cold rolling, the total increase in the B2 fraction during annealing is 3–6% (from 31% [29] to 34–37%, see Fig. 7). This increase can be attributed to precipitation of B2 particles during the heat-treatment. The
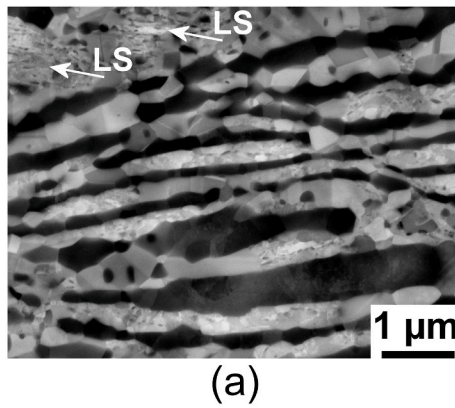
Fig. 3. Microstructure of the sample annealed for 2.5 min at 800 °C observed using SEM-based techniques: (a) BSE image where B2 regions typically appear darker than FCC regions. Arrows in (a) indicate examples of regions containing non-recrystallized lamellar structures (LS); (b,c) phase maps collected using the EBSD technique (only areas identified as recrystallized grains are shown in (c)). In (b,c) FCC and B2 regions are shown in red and blue, respectively. White, black and yellow lines indicate LABs, HABs and twin boundaries, respectively. The RD is parallel to the scale bars. (For interpretation of the references to colour in this figure legend, the reader is referred to the Web version of this article.)
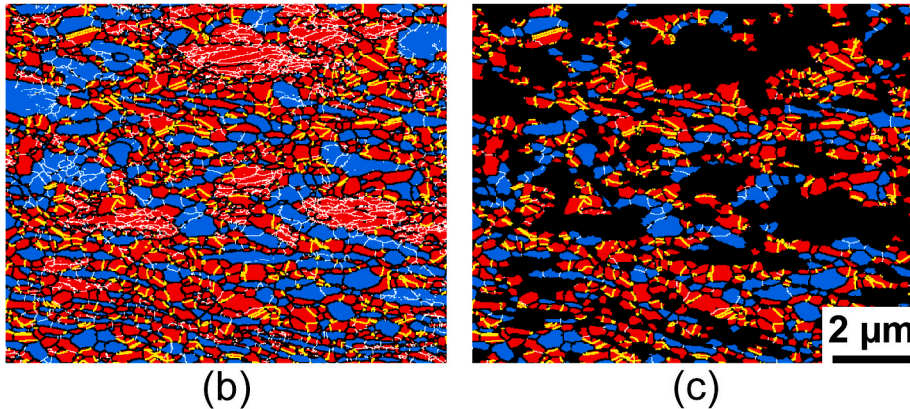
phase fractions in the annealed samples presented in Fig. 7 are different from those in Refs. [25,26], where fractions of the FCC and B2 phases after annealing at 800 °C for 1 h were reported to be 55% and 45%, respectively. The different proportion of the phases reported in Refs. [25,26] may be due to the smaller areas analyzed there, although the differences in the initial as-cast microstructures may also play a role (see Section 2).

3.2. Texture

Fig. 8 shows crystallographic textures presented in terms of orientation distribution functions (ODF), calculated separately for non-recrystallized and recrystallized regions in the sample annealed for 2.5 min at 800 °C. In the non-recrystallized FCC phase, most orientations are along the $\langle 110 \rangle$//ND fiber, with the maximum intensity near the brass (Bs) $\{110\}\langle 112 \rangle$ component (see Fig. 8a). The intensity of the Goss (G) $\{110\}\langle 001 \rangle$ component is also significant in this fiber. The other standard components of the rolling texture in FCC materials, S $\{123\}\langle 634 \rangle$ and copper (Cu) $\{112\}\langle 111 \rangle$, are associated with low intensities in the ODF. The texture of the non-recrystallized B2 regions (Fig. 8b) is represented by a strong $\langle 111 \rangle$//ND fiber with a high intensity of the $\{111\}\langle 110 \rangle$ component.

For each phase, the dominant texture fibers are slightly weaker in recrystallized microstructure than in the non-recrystallized regions (cf. Fig. 8c and d and Fig. 8a and b). Considering the overall texture evolution during recrystallization, the fraction of the $\langle 110 \rangle$//ND fiber in the FCC phase and the fraction of the $\langle 111 \rangle$//ND fiber in the B2 phase both increase with increasing annealing duration (see Fig. 9).

3.3. Mechanical behavior

Tensile test data show that the cold-rolled sample has a high 0.2% proof stress, $\sigma_{0.2} = 1517$ MPa, and an ultimate tensile strength approaching 2000 MPa (see Fig.10a,c). After reaching the maximum

stress σ_m this sample demonstrates a reduction in the engineering stress due to local necking (see Appendix A for fractography). In the rolled condition, the work hardening capacity (WHC), defined as $\sigma_m - \sigma_{0.2}$, is high (see Fig. 10d), and the elongation to failure ε_f is ~8%.

Annealing at 800 °C decreases both strength and WHC (Fig. 10c and d), while ε_f increases. As is evident from Fig. 10c, changes in tensile strength and ε_f are rapid within the first 10 min at 800 °C, followed by a slower evolution during further annealing. Nevertheless, the strength is still fairly high even after annealing for 2 h, $\sigma_{0.2} = 1237$ MPa and $\sigma_m = 1367$ MPa. The elongation to failure in this annealed sample is 17%. It is noteworthy that the annealed samples failed at (or almost at) the maximum stress with no clear evidence of local necking.

A closer inspection of the stress-strain curves reveals additional differences between the cold-rolled and annealed samples. In particular, while the engineering stress for the cold-rolled material increases continuously until the onset of necking, the stress-strain curve for the sample annealed for 2.5 min is characterized by the presence of a short plateau where the stress is almost constant (shown in more detail in Fig. 10b), after which work-hardening is resumed. Furthermore, for the sample annealed for 5 min, a small yield drop of 6 MPa (averaged over 3 tested specimens) is seen soon after the onset of plastic deformation (Fig. 10b). The yield drop becomes more pronounced after extended annealing, being 45 MPa in the sample annealed for 2 h.

Distributions of local strains and local strain rates in two partially recrystallized conditions with either a small yield drop or a significant yield drop (samples annealed for 5 min and 30 min, respectively) are shown in Fig. 11. DIC images presented in this figure correspond to different engineering strains labeled by letters on the stress-strain curves. A small decrease in stress observed after point B in Fig. 11a (illustrating the data for the sample annealed for 5 min) is related to strain localization in the form of a propagating Lüders band. The moving front of the band can be seen more clearly in the strain-rate maps at points B and C (total strains of 1.9% and 4%, respectively). Further plastic deformation of this sample is accompanied by work-hardening
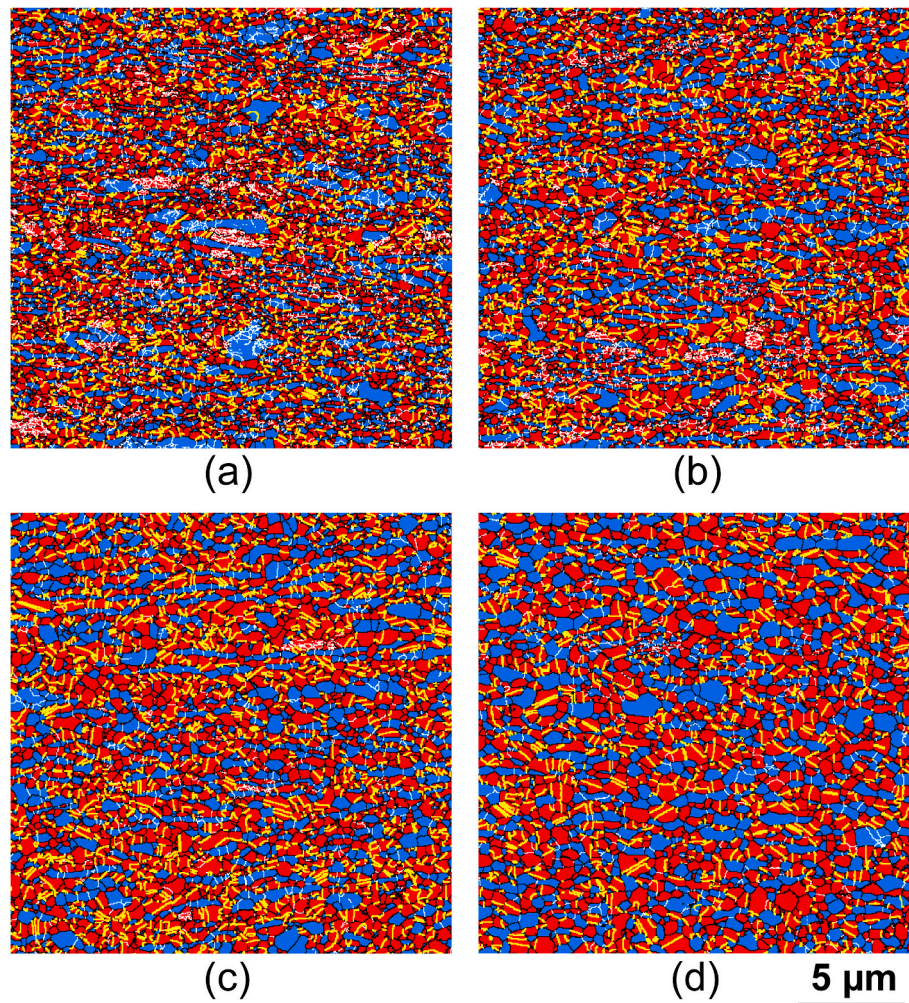
Fig. 4. Phase maps representing the microstructure of the samples annealed at 800 °C for 5 min (a); 10 min (b); 30 min (c); 2 h (d). FCC and B2 regions are shown in red and blue, respectively. White, black and yellow lines indicate LABs, HABs and twin boundaries, respectively. The RD is parallel to the scale bar. (For interpretation of the references to colour in this figure legend, the reader is referred to the Web version of this article.)
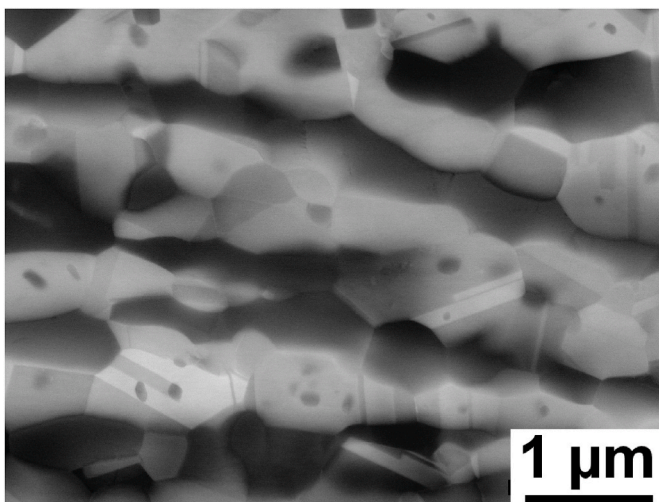

Fig. 5. BSE image showing the microstructure in the sample annealed for 30 min at 800 °C. Note the presence of fine isolated B2 crystallites seen as dark features within and between brighter recrystallized FCC grains.

until fracture with no indication of intense Lüders banding (see DIC data at point D in Fig. 11a and a video clip in Supplementary Content). The data for the sample annealed for 30 min (Fig. 11b) show a well-defined upper yield point near A followed by a sharp yield drop and Lüders banding. Lüders deformation proceeds in this sample to point D (7.5% strain) where the band has propagated along the entire gauge length of the specimen. Overall, the Lüders strain in the 30-min sample is larger than that in the 5-min sample.

Supplementary video related to this article can be found at htt ps://doi.org/10.1016/j.msea.2021.142558

4. Discussion

4.1. Effect of rolling on lamella thickness

It is known that FCC(L1$_2$) regions in the as-cast AlCoCrFeNi$_{2.1}$ alloy are significantly softer than B2 regions [27]. Taking into account that during heavy rolling the initially softer phase is expected to accommodate a higher strain than the harder phase, it is not surprising that finely spaced lamellar boundaries are observed within deformed FCC volumes (see Fig. 1b). The extent of deformation-induced subdivision can be evaluated from comparison of microstructural features in the as-cast and rolled samples. The average thickness of FCC(L1$_2$) lamellae and
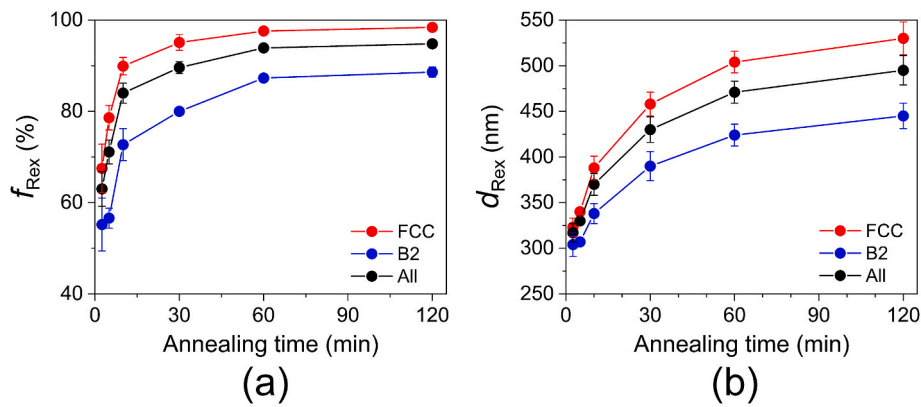
Fig. 6. Parameters of recrystallized grains identified by the EBSD analysis of the samples annealed at 800 °C: (a) recrystallized area fraction f_{Rex} (data for the FCC and B2 phases represent recrystallized fractions calculated separately within each phase); (b) average recrystallized grain size d_{Rex} calculated ignoring twin boundaries.
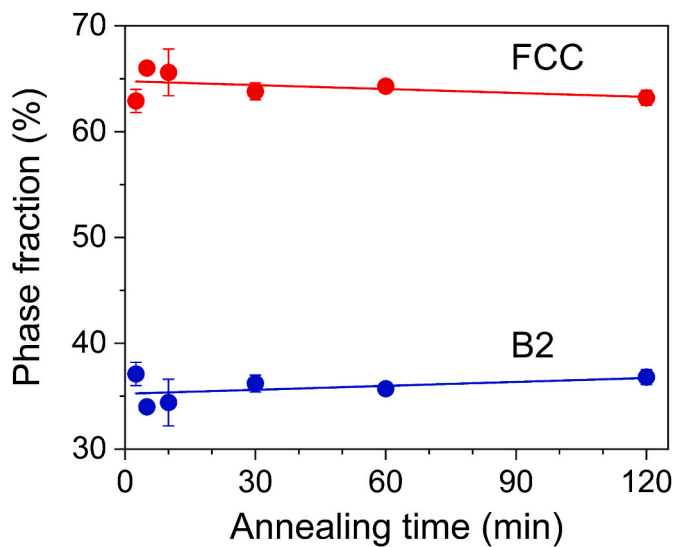

Fig. 7. Area fractions of FCC and B2 phases determined by EBSD in the samples annealed at 800 °C.

non-lamellar regions in the as-cast sample was measured to be 700 nm and 1160 nm, respectively [29]. From geometrical considerations, in the 90% rolled sample this thickness is expected to be reduced to 70 nm and 116 nm, respectively. Considering that the average boundary spacing in the FCC phase of the deformed sample is only 30 nm, it can be suggested that individual FCC(L1$_2$) volumes present in the as-cast sample were subdivided into 2 to 4 lamellae by heavy rolling.

Although fine B2 lamellae are also present in the deformed microstructure, the average thickness of microstructural features of the B2 phase is much greater, 130 nm, than the interlamellar spacing within the FCC regions. As the average thickness of B2 lamellae and irregular B2 features in the as-cast material was 350 nm and 590 nm, respectively [29], it is obvious that their thickness reduction is less than that anticipated due to 90% rolling. Since B2 regions are less deformed than FCC regions, it is reasonable to conclude that the stored energy in the B2 phase is significantly lower than in the FCC phase.

4.2. Development and kinetics of recrystallization

Obviously, the driving pressure for recrystallization is higher in regions with a higher stored energy. Therefore, recrystallization during annealing proceeds much faster in the FCC phase than in the B2 phase (Fig. 6a). The size of recrystallized FCC grains after 2.5 min at 800 °C is an order of magnitude greater than the FCC lamellar spacing in the

deformed microstructure. This implies that many FCC nuclei grow initially by *grain boundary* migration within FCC regions. In contrast, in the less subdivided B2 phase, coarsening is constrained by phase boundaries already at the initial stage of recrystallization. As a result, B2 grains can grow to a relatively large size only if migration of *phase boundaries* is involved. During extended annealing at 800 °C, the migration of phase boundaries results in break-up of the lamellar morphology, with only residual directionality seen in the microstructure annealed for 2 h (Fig. 4d).

The overall recrystallization kinetics in the annealed material can be analyzed using a Johnson–Mehl–Avrami–Kolmogorov (JMAK) plot which presents -ln(1-f_{Rex}) as a function of annealing time t on a double logarithmic scale. The Avrami exponent n in the classical equation f_{Rex} = 1-exp(-Kt^n), where K is a constant, can be then derived from the slope in the JMAK plot, as shown in Fig. 12. For the samples analyzed in the present experiment, the obtained Avrami exponent is small, n = 0.29. Such a small value of the Avrami exponent can be due to the presence of two phases recrystallizing at different rates, with recrystallization being slower in the B2 phase. Similar results were obtained for Cu processed by dynamic plastic deformation, where alternating bands of low and high stored energies recrystallized at very different rates [34]. The presence of phase boundaries can further limit the growth dimension, and thus additionally reduce the Avrami exponent. Small Avrami exponents (n = 0.22–0.52) were also reported for an Al$_{0.3}$CoCrFeNi HEA, in which recrystallization and precipitation of the B2 phase took place during annealing of cold-rolled samples [33].

The EBSD analysis indicates that the average recrystallized grain size d_{Rex} in each AlCoCrFeNi$_{2.1}$ sample annealed at 800 °C is much smaller than the critical nucleus radius of 1 μm in the classical theory of recrystallization developed for single-phase materials [35]. Apparently, the very small grain size in the annealed EHEA is closely related to the extremely fine deformation structure obtained by heavy rolling. It is suggested that the complex chemical composition of this alloy and its dual-phase structure hinder dynamic recovery and coarsening during deformation, leading to the small average interlamellar spacing at least in the FCC phase. Annealing at 800 °C generates a high frequency of tiny recrystallization nuclei, which results in ultrafine grains (d_{Rex} = 0.5 μm) when recrystallization is almost complete. As follows from previous experiments on the AlCoCrFeNi$_{2.1}$ alloy, the growth of recrystallized grains in this material is restricted also at temperatures considerably higher than 800 °C. For example, it has been shown that the average grain size in this alloy is <1 μm even after annealing at 1000 °C for 1 h [25,36]. This indicates that truly ultrafine-grained (UFG) samples can be obtained in this alloy during recrystallization within a wide temperature range.

Recrystallization textures in the AlCoCrFeNi$_{2.1}$ alloy demonstrate two strong fibers, ⟨110⟩//ND in the FCC phase and ⟨111⟩//ND in the B2
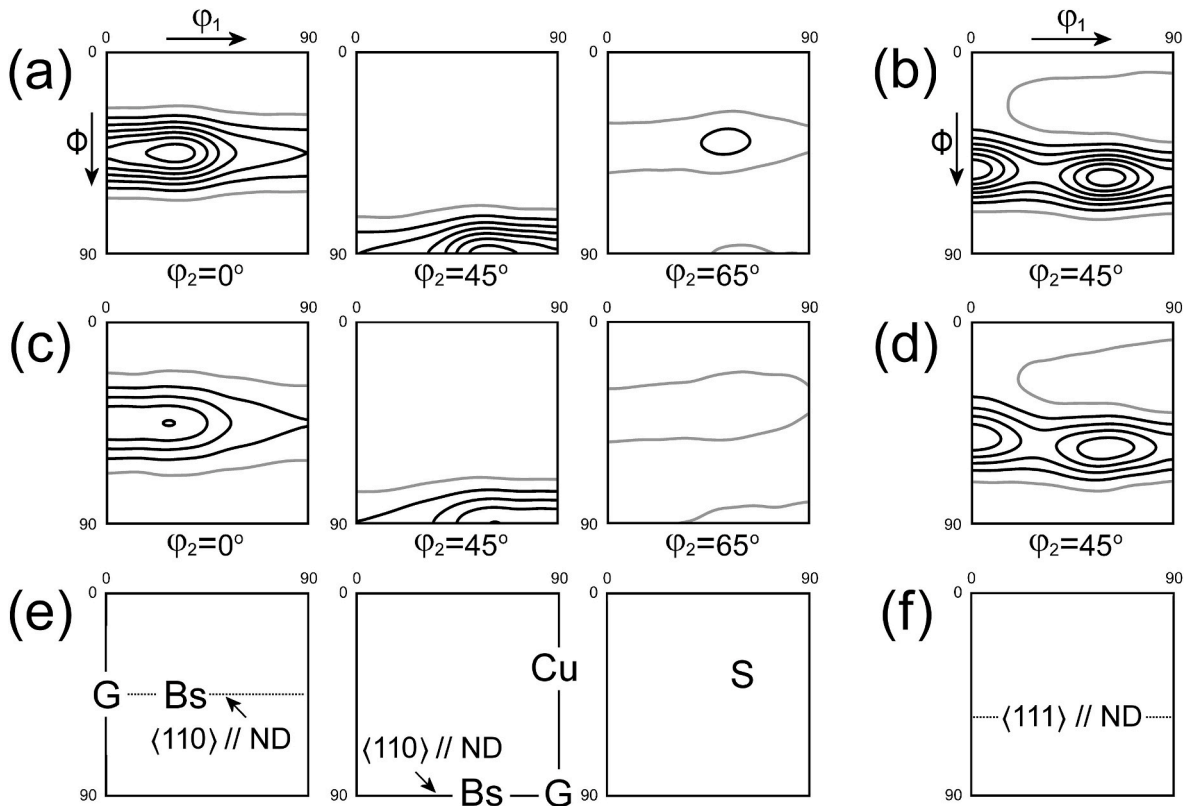
Fig. 8. Sections of ODFs calculated from the EBSD data for the sample annealed for 2.5 min at 800 °C: (a) non-recrystallized FCC regions; (b) non-recrystallized B2 regions; (c) recrystallized FCC regions; (d) recrystallized B2 regions. Contour levels are 1, 2, 3, 4, 5, 6, 7 × random. Positions of the ⟨110⟩//ND fiber and the standard rolling texture components in FCC materials are shown in (e). Position of the ⟨111⟩//ND fiber pronounced in the B2 phase is shown in (f).
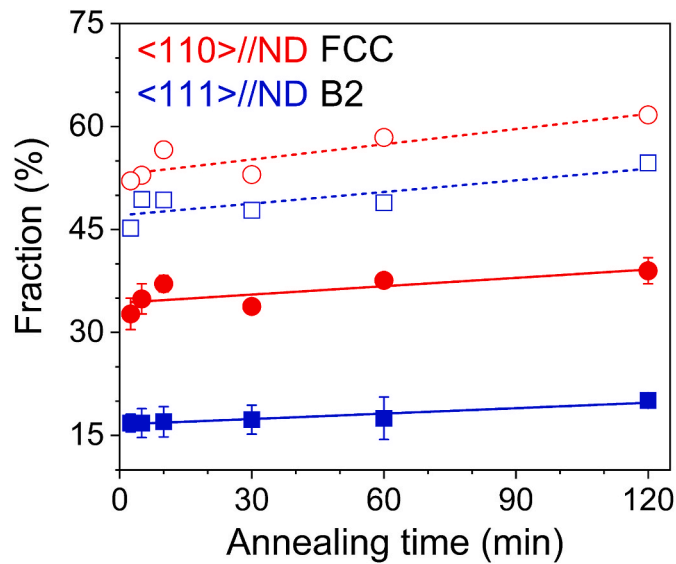

Fig. 9. Area fractions of texture fibers calculated from the EBSD data. Solid symbols indicate fractions calculated based on all orientations present in each data set, while open symbols indicate texture fractions normalized by the number of pixels of each phase.
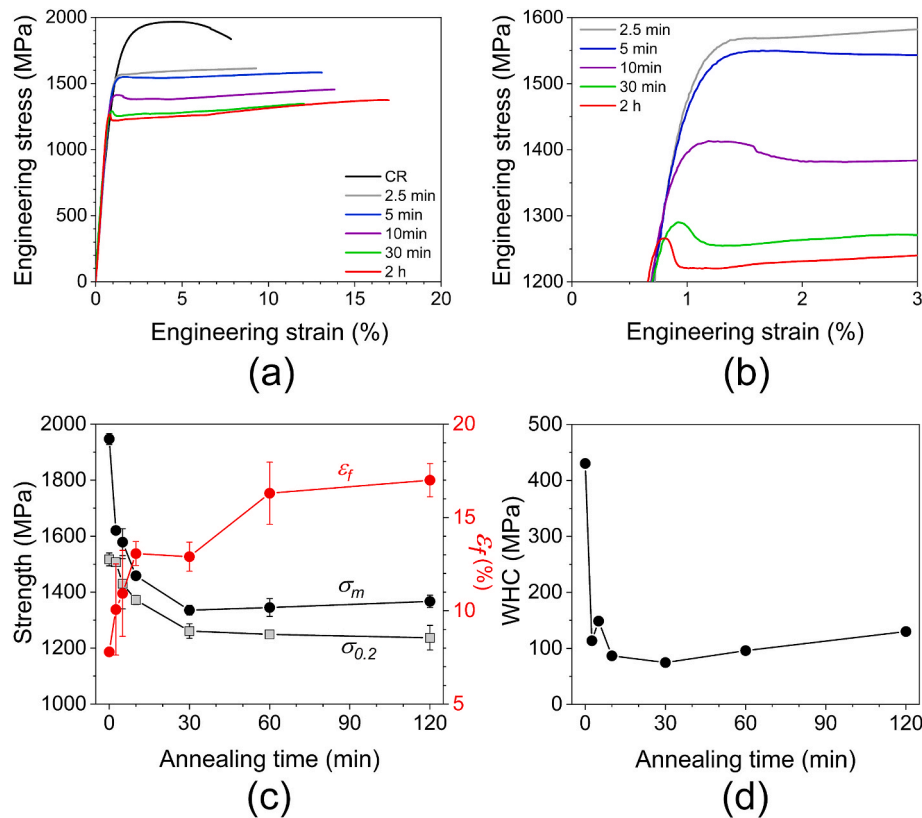
Fig. 10. Tensile test data for the cold-rolled (CR) sample and samples annealed at 800 °C for different periods of time: (a) complete stress-strain curves; (b) low-strain region of the curves for the annealed samples; (c) evolution of strength and elongation to failure as a function of annealing time; (d) work hardening capacity (WHC) defined as $\sigma_m - \sigma_{0.2}$.

phase (Fig. 8), which are characteristic fibers in rolled FCC materials with low stacking fault energies and rolled BCC materials, respectively [37,38]. The presence of these fibers in the recrystallization texture of AlCoCrFeNi$_{2.1}$ suggests that annealing resulted in a high frequency of nuclei having orientations of the deformed matrix. However, the texture of recrystallized grains is not fully identical to the texture of the non-recrystallized regions as is seen in the sample annealed for 2.5 min at 800 °C (cf. Fig. 8a,b and Fig. 8c,d). In this sample, the major rolling texture components are weaker in the recrystallization texture, which implies that grain orientations deviating from the orientations of the rolling texture have a certain advantage during nucleation within the first 2.5 min of annealing. Further annealing at 800 °C leads to nucleation in the remaining non-recrystallized regions and to some growth of the earlier recrystallized grains, accompanied by a small increase in the fraction of the dominant fibers (Fig. 9).

4.3. Evolution of mechanical properties during annealing

The cold-rolled AlCoCrFeNi$_{2.1}$ sample has the highest strength and the lowest ductility, which reflects the fine boundary spacing and high dislocation density observed in the as-deformed microstructure. Recrystallization reduces strength and improves ductility, while precipitation of B2 particles counteracts the loss of strength. Considering the tensile test data in Fig. 10c, combinations of high yield strength and good ductility are observed in the samples annealed for 2.5–10 min, where the total fraction of non-recrystallized regions is still substantial. In these samples, $\sigma_{0.2}$ is 1372 MPa to 1507 MPa, and ε_f is 10% to 13%.

Strength-ductility combinations obtained in this work are compared in Fig. 13 with the literature data available for several other AlCoCrFeNi$_{2.1}$ samples in the as-cast, rolled and annealed conditions [24–28, 36,39]. It is significant that the as-cast samples (encircled data points) are characterized by elongations of 16–17% and comparatively low

yield strength (500–650 MPa), whereas any thermomechanically processed sample with similar ductility also has a much higher strength. This highlights the benefit of thermomechanical processing for improved mechanical performance of the AlCoCrFeNi$_{2.1}$ alloy. The data for the rolled and annealed samples show a large scatter due to the different processing routes used in the different experiments. Nevertheless, the majority of the data points for such samples demonstrate an almost linear decline in strength as ductility improves. In general, our data follow this behavior; however, for elongations in the range 10–15% the partially recrystallized samples have considerably higher yield strengths than the fully recrystallized samples [25–27] with similar ε_f. Therefore, there is a clear potential to expand the range of strength-ductility combinations via partial recrystallization.

It is noteworthy that one data set [28] shows an exceptionally good combination of high strength and high ductility. This combination can be attributed to an increased frequency of precipitates due to slow heating applied prior to annealing [28] as compared to the largely isothermal heat treatments used in several other experiments. It is expected that the mechanical behavior of partially recrystallized HEAs can be further improved through control of the heating rate.

One particularly interesting result obtained in the present work is that the increased ductility due to recrystallization does not lead to increased WHC as compared to the cold-rolled sample (see Fig. 10d). It is believed that the high WHC of the cold-rolled material is enabled predominantly by the less deformed B2 phase, which can retain a greater ability to work-harden during tensile testing than the severely strained FCC phase. It should, however, be noted that the WHC of cold-rolled AlCoCrFeNi$_{2.1}$ samples used in different experiments was not identical. Table 1 shows that the WHC of the rolled sample studied in the present work is greater than that of the rolled material investigated by Wani et al. [25,26]. The different WHC is likely caused by differences in their as-cast microstructures, and hence also in deformed
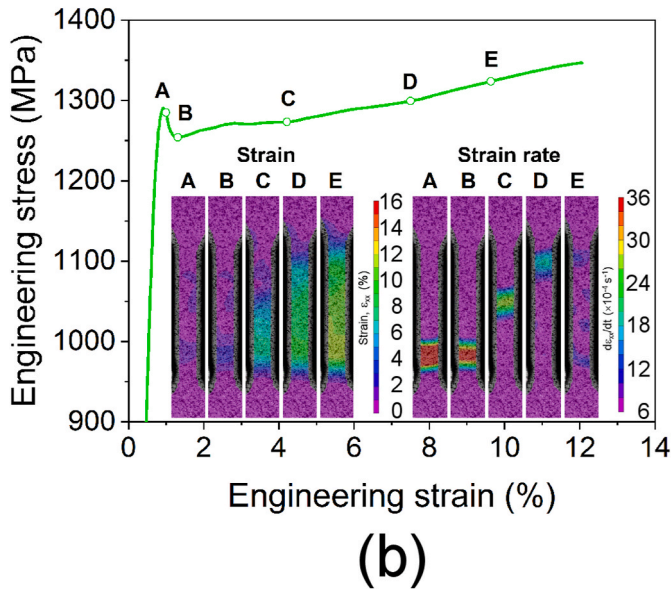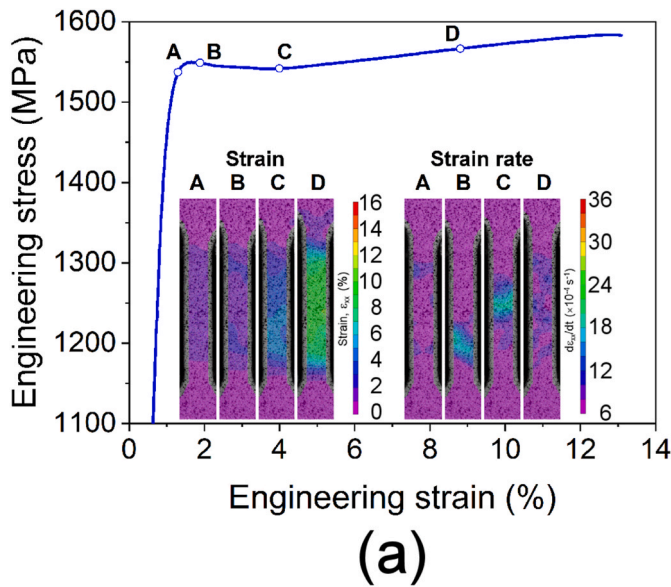
Fig. 12. JMAK plot for the samples annealed at 800 °C. The Avrami exponent determined from the plot is 0.29.

Fig. 11. DIC data showing local strains and local strain rates measured during tensile tests: (a) sample annealed at 800 °C for 5 min; (b) sample annealed at 800 °C for 30 min. Each DIC image corresponds to a certain location on the stress-strain curve (locations are marked by letters).

Fig. 13. Combinations of yield strength and ductility for the samples studied in the present work and for other AlCoCrFeNi$_{2.1}$ samples described in several previous publications. Encircled data points correspond to as-cast samples.

microstructures. Thinner ingots had finer lamellae in the as-cast material and finer boundary spacing after rolling [25,26], which resulted in a higher yield strength and lower WHC than those of the cold-rolled sample investigated here. Nevertheless, the WHC of the cold-rolled sample from Refs. [25,26] is still greater than the WHC of the samples annealed at 800 °C (see Table 1 and Fig. 10d). The low WHC of these annealed samples is attributed to a reduced ability to accumulate dislocations inside recrystallized ultrafine grains [40–43]. As the annealing time at 800 °C is extended, or as the annealing temperature is increased, the WHC increases due to a larger average recrystallized grain size (see Table 1). These observations of the grain size effect in AlCoCrFeNi$_{2.1}$ are consistent with results obtained on single-phase FCC HEAs [44,45].

The yield drop phenomenon observed in the samples annealed for at least 5 min (see Fig. 10a and b) is closely related to the lack of mobile dislocations. For these samples, a high initial stress is required to activate dislocation sources and generate new mobile dislocations in the microstructure, as is also reported for metals and conventional alloys
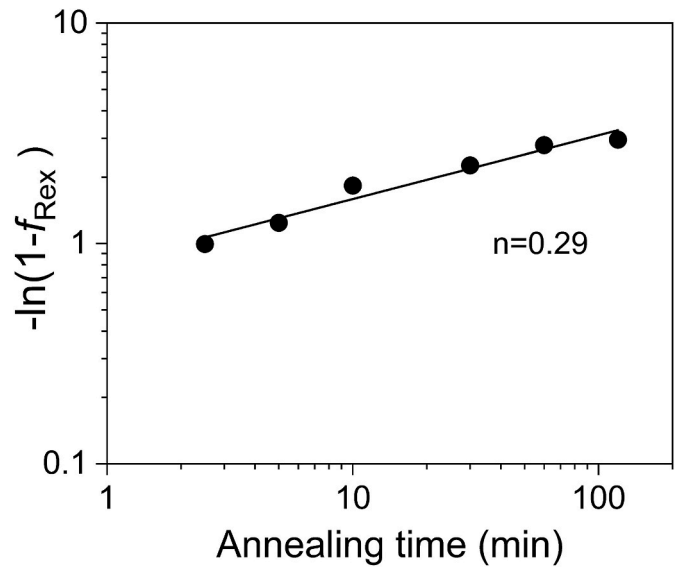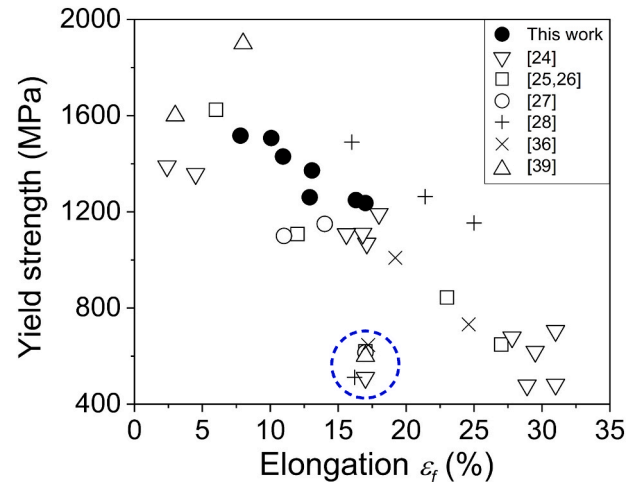
with UFG microstructures [40–43,46]. As soon as the dislocation density increases, the stress needed to maintain the applied strain rate decreases, which results in the observed yield drop, with further plastic deformation taking place by propagation of Lüders bands. After one or several bands have propagated through the gauge zone of the specimens, the material work-hardens continuously until failure.

For the material studied in the present work, it can be shown that there is a correlation between the magnitude of the yield drop Δσ and the recrystallized area fraction f_{Rex}. This correlation is evident from Fig. 14, which shows that Δσ increases with increasing f_{Rex}, i.e., with decreasing fraction of the microstructure containing a high dislocation density. Assuming a linear relationship between Δσ and f_{Rex}, it can be expected that there will be no yield drop in annealed AlCoCrFeNi$_{2.1}$ at f_{Rex} below 67%. The fact that the yield drop is not seen for the sample annealed for 2.5 min with $f_{Rex} = 63\%$ is therefore in agreement with this expected result.

Table 1
Microstructural parameters[1], strength and WHC of different AlCoCrFeNi$_{2.1}$ samples produced by 90% cold rolling (CR) and subsequent annealing at 800 °C, 1000 °C and 1200 °C for 1 h.

Sample	d_{Rex} (μm)	f_{Rex} (%)	$\sigma_{0.2}$ (MPa)	σ_m (MPa)	WHC (MPa)
CR90%	–	–	1517	1947	430
CR90% [25,26]	–	–	1625	1800	175
CR90% + 1 h at 800 °C	0.5	93	1249	1345	96
CR90% + 1 h at 800 °C [25,26]	0.5	100	1108	1200	92
CR90% + 1 h at 1000 °C [25]	0.8	100	844	1175	331
CR90% + 1 h at 1200 °C [25]	2.0	100	648	1075	427

[1]For samples studied in Refs. [25,26], d_{Rex} was calculated based on average grain sizes reported for individual phases and their area fractions. Recrystallization was reported to be complete for the sample annealed at 800 °C for 1 h [26] and is apparently complete for the samples annealed at the higher temperatures [25].
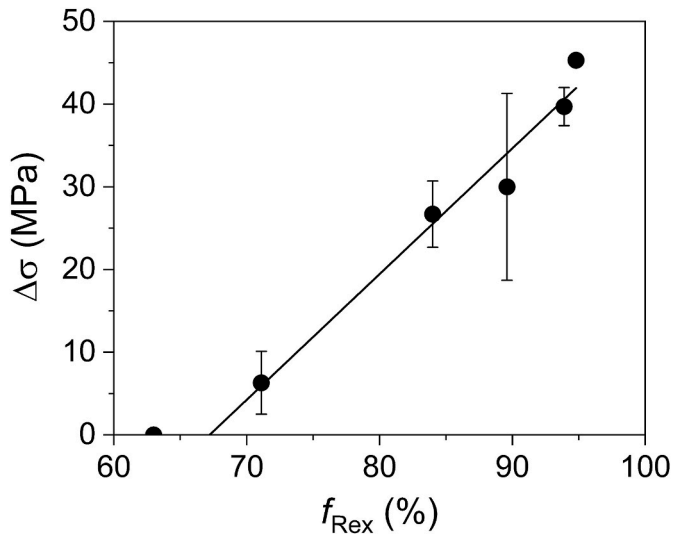

Fig. 14. The magnitude of yield drop $\Delta\sigma$ vs fraction recrystallized f_{Rex} in the AlCoCrFeNi$_{2.1}$ alloy annealed at 800 °C.

5. Conclusions

1. Significant differences in the microstructure of FCC and B2 regions are found in 90% cold-rolled AlCoCrFeNi$_{2.1}$. The FCC phase appears more deformed than the B2 regions and contains a high frequency of finely spaced deformation-induced boundaries, which provides a higher driving force for recrystallization within the FCC phase.
2. Quantitative EBSD analysis of microstructural changes taking place in the cold-rolled material annealed at 800 °C indicates that in the FCC phase recrystallization progresses faster and with a larger recrystallized grain size than in the B2 phase. The average recrystallized size is in the submicron range (0.5 μm) even after annealing for 2 h at 800 °C. The fraction of the ⟨110⟩//ND fiber in the FCC phase and the fraction of the ⟨111⟩//ND fiber in the B2 phase both increase between 2.5 min and 2 h of annealing.
3. The cold-rolled sample demonstrates the highest tensile strength and lowest ductility. Recrystallization results in reduced strength and improved ductility, with good strength-ductility combinations in the samples annealed at 800 °C for 2.5–10 min. In these samples, the 0.2% proof stress is 1372 MPa to 1507 MPa, and the elongation to failure is 10% to 13%. The work-hardening capacity of each annealed sample is lower than that of the cold-rolled sample.
4. Samples annealed at 800 °C for at least 5 min develop a yield drop soon after the onset of plastic deformation. The magnitude of the yield drop varies from 6 MPa in the sample annealed for 5 min to 45 MPa in the sample annealed for 2 h. For the annealed samples, a clear correlation is observed between the magnitude of the yield drop and the recrystallized fraction.

CRediT authorship contribution statement

Adrianna Lozinko: Methodology, Investigation, Formal analysis, Writing – original draft. **Reza Gholizadeh:** Investigation, Formal analysis, Writing – review & editing. **Yubin Zhang:** Investigation, Writing – review & editing. **Uta Klement:** Writing – review & editing. **Nobuhiro Tsuji:** Writing – review & editing. **Oleg V. Mishin:** Conceptualization, Methodology, Investigation, Formal analysis, Writing – original draft. **Sheng Guo:** Conceptualization, Resources, Writing – review & editing, Supervision.

Declaration of competing interest

The authors declare that they have no known competing financial interests or personal relationships that could have appeared to influence the work reported in this paper.

Data availability

The raw/processed data required to reproduce these findings cannot be shared at this time as the data also forms part of an ongoing study.

Appendix A. Supplementary data

Supplementary data to this article can be found online at https://doi.org/10.1016/j.msea.2021.142558.

References

[1] B. Gludovatz, A. Hohenwarter, D. Catoor, E.H. Chang, E.P. George, R.O. Ritchie, A fracture-resistant high-entropy alloy for cryogenic applications, Science 345 (2014) 1153–1158, https://doi.org/10.1126/science.1254581.
[2] Z. Li, K.G. Pradeep, Y. Deng, D. Raabe, C.C. Tasan, Metastable high-entropy dual-phase alloys overcome the strength-ductility trade-off, Nature 534 (2016) 227–230, https://doi.org/10.1038/nature17981.
[3] Z.J. Zhang, M.M. Mao, J. Wang, B. Gludovatz, Z. Zhang, S.X. Mao, E.P. George, Q. Yu, R.O. Ritchie, Nanoscale origins of the damage tolerance of the high-entropy alloy CrMnFeCoNi, Nat. Commun. 6 (2015) 1–6, https://doi.org/10.1038/ncomms10143.

[4] L. Zhang, Y. Zhou, X. Jin, X. Du, B. Li, Precipitation-hardened high entropy alloys with excellent tensile properties, Mater. Sci. Eng. A 732 (2018) 186–191, https://doi.org/10.1016/j.msea.2018.06.102.

[5] M.J.J. Yao, K.G.G. Pradeep, C.C.C. Tasan, D. Raabe, A novel, single phase, non-equiatomic FeMnNiCoCr high-entropy alloy with exceptional phase stability and tensile ductility, Scripta Mater. 72–73 (2014) 5–8, https://doi.org/10.1016/j.scriptamat.2013.09.030.

[6] J.Y. He, H. Wang, H.L. Huang, X.D. Xu, M.W. Chen, Y. Wu, X.J. Liu, T.G. Nieh, K. An, Z.P. Lu, A precipitation-hardened high-entropy alloy with outstanding tensile properties, Acta Mater. 102 (2016) 187–196, https://doi.org/10.1016/j.actamat.2015.08.076.

[7] Q. Wang, Y. Ma, B. Jiang, X. Li, Y. Shi, C. Dong, P.K. Liaw, A cuboidal B2 nanoprecipitation-enhanced body-centered-cubic alloy Al0.7CoCrFe2Ni with prominent tensile properties, Scripta Mater. 120 (2016) 85–89, https://doi.org/10.1016/j.scriptamat.2016.04.014.

[8] K. Ming, X. Bi, J. Wang, Precipitation strengthening of ductile $Cr_{15}Fe_{20}Co_{35}Ni_{20}Mo_{10}$ alloys, Scripta Mater. 137 (2017) 88–93, https://doi.org/10.1016/j.scriptamat.2017.05.019.

[9] Y. Tong, D. Chen, B. Han, J. Wang, R. Feng, T. Yang, C. Zhao, Y.L. Zhao, W. Guo, Y. Shimizu, C.T. Liu, P.K. Liaw, K. Inoue, Y. Nagai, A. Hu, J.J. Kai, Outstanding tensile properties of a precipitation-strengthened FeCoNiCrTi0.2 high-entropy alloy at room and cryogenic temperatures, Acta Mater. 165 (2019) 228–240, https://doi.org/10.1016/j.actamat.2018.11.049.

[10] L.J. Zhang, K. Guo, H. Tang, M.D. Zhang, J.T. Fan, P. Cui, Y.M. Ma, P.F. Yu, G. Li, The microstructure and mechanical properties of novel Al-Cr-Fe-Mn-Ni high-entropy alloys with trimodal distributions of coherent B2 precipitates, Mater. Sci. Eng. A 757 (2019) 160–171, https://doi.org/10.1016/j.msea.2019.04.104.

[11] Z. Li, L. Fu, J. Peng, H. Zheng, X. Ji, Y. Sun, S. Ma, A. Shan, Improving mechanical properties of an FCC high-entropy alloy by γ′ and B2 precipitates strengthening, Mater. Char. 159 (2020), https://doi.org/10.1016/j.matchar.2019.109989, 109989.

[12] Z. Li, C.C. Tasan, K.G. Pradeep, D. Raabe, A TRIP-assisted dual-phase high-entropy alloy: grain size and phase fraction effects on deformation behavior, Acta Mater. 131 (2017) 323–335, https://doi.org/10.1016/j.actamat.2017.03.069.

[13] D.G. Kim, Y.H. Jo, J. Yang, W.M. Choi, H.S. Kim, B.J. Lee, S.S. Sohn, S. Lee, Ultrastrong duplex high-entropy alloy with 2 GPa cryogenic strength enabled by an accelerated martensitic transformation, Scripta Mater. 171 (2019) 67–72, https://doi.org/10.1016/j.scriptamat.2019.06.026.

[14] Z. Li, F. Körmann, B. Grabowski, J. Neugebauer, D. Raabe, Ab initio assisted design of quinary dual-phase high-entropy alloys with transformation-induced plasticity, Acta Mater. 136 (2017) 262–270, https://doi.org/10.1016/j.actamat.2017.07.023.

[15] H. Huang, Y. Wu, J. He, H. Wang, X. Liu, K. An, W. Wu, Z. Lu, Phase-transformation ductilization of brittle high-entropy alloys via metastability engineering, Adv. Mater. 29 (2017) 1–7, https://doi.org/10.1002/adma.201701678.

[16] Y.H. Jo, D.G. Kim, M.C. Jo, K.Y. Doh, S.S. Sohn, D. Lee, H.S. Kim, B.J. Lee, S. Lee, Effects of deformation–induced BCC martensitic transformation and twinning on impact toughness and dynamic tensile response in metastable VCrFeCoNi high–entropy alloy, J. Alloys Compd. 785 (2019) 1056–1067, https://doi.org/10.1016/j.jallcom.2019.01.293.

[17] R.R. Eleti, M. Klimova, M. Tikhonovsky, N. Stepanov, S. Zherebtsov, Exceptionally high strain-hardening and ductility due to transformation induced plasticity effect in Ti-rich high-entropy alloys, Sci. Rep. 10 (2020) 13293, https://doi.org/10.1038/s41598-020-70298-2.

[18] I. Baker, M. Wu, Z. Wang, Eutectic/eutectoid multi-principle component alloys: a review, Mater. Char. 147 (2019) 545–557, https://doi.org/10.1016/j.matchar.2018.07.030.

[19] Y. Lu, H. Jiang, S. Guo, T. Wang, Z. Cao, T. Li, A new strategy to design eutectic high-entropy alloys using mixing enthalpy, Intermetallics 91 (2017) 124–128, https://doi.org/10.1016/j.intermet.2017.09.001.

[20] Wang, B. Wen, Z. Wang, J. Jie, Z. Cao, H. Ruan, T. Li, A promising new class of high-temperature alloys: eutectic high-entropy alloys, Sci. Rep. 4 (2014) 6200, https://doi.org/10.1038/srep06200.

[21] Y. Lu, X. Gao, L. Jiang, Z. Chen, T. Wang, J. Jie, H. Kang, Y. Zhang, S. Guo, H. Ruan, Y. Zhao, Z. Cao, T. Li, Directly cast bulk eutectic and near-eutectic high entropy alloys with balanced strength and ductility in a wide temperature range, Acta Mater. 124 (2017) 143–150, https://doi.org/10.1016/j.actamat.2016.11.016.

[22] X. Gao, Y. Lu, B. Zhang, N. Liang, G. Wu, G. Sha, J. Liu, Y. Zhao, Microstructural origins of high strength and high ductility in an AlCoCrFeNi2.1 eutectic high-entropy alloy, Acta Mater. 141 (2017) 59–66, https://doi.org/10.1016/j.actamat.2017.07.041.

[23] Y. Zhang, J. Li, X. Wang, Y. Lu, Y. Zhou, X. Sun, The interaction and migration of deformation twin in an eutectic high-entropy alloy AlCoCrFeNi2.1, J. Mater. Sci. Technol. 35 (2019) 902–906, https://doi.org/10.1016/j.jmst.2018.09.067.

[24] S.R. Reddy, U. Sunkari, A. Lozinko, R. Saha, S. Guo, P.P. Bhattacharjee, Microstructural design by severe warm-rolling for tuning mechanical properties of AlCoCrFeNi2.1 eutectic high entropy alloy, Intermetallics 114 (2019) 106601, https://doi.org/10.1016/j.intermet.2019.106601.

[25] I.S. Wani, T. Bhattacharjee, S. Sheikh, P.P. Bhattacharjee, S. Guo, N. Tsuji, Tailoring nanostructures and mechanical properties of AlCoCrFeNi2.1 eutectic high

[26] I.S. Wani, T. Bhattacharjee, S. Sheikh, Y.P. Lu, S. Chatterjee, P.P. Bhattacharjee, S. Guo, N. Tsuji, Ultrafine-grained AlCoCrFeNi2.1 eutectic high-entropy alloy, Mater. Res. Lett. 4 (2016) 174–179, https://doi.org/10.1080/21663831.2016.1160451.

[27] T. Bhattacharjee, I.S. Wani, S. Sheikh, I.T. Clark, T. Okawa, S. Guo, P.P. Bhattacharjee, N. Tsuji, Simultaneous strength-ductility enhancement by cryo-rolling and annealing of a nano-lamellar AlCoCrFeNi2.1 eutectic high entropy alloy, Sci. Rep. 8 (2018) 3276, https://doi.org/10.1038/s41598-018-21385-y.

[28] P. Shi, W. Ren, T. Zheng, Z. Ren, X. Hou, J. Peng, P. Hu, Y. Gao, Y. Zhong, P.K. Liaw, Enhanced strength–ductility synergy in ultrafine-grained eutectic high-entropy alloys by inheriting microstructural lamellae, Nat. Commun. 10 (2019) 1–8, https://doi.org/10.1038/s41467-019-08460-2.

[29] A. Lozinko, O.V. Mishin, T. Yu, U. Klement, S. Guo, Y. Zhang, Quantification of microstructure in a eutectic high entropy alloy AlCoCrFeNi2.1, IOP Conf. Ser. Mater. Sci. Eng. 580 (2019), https://doi.org/10.1088/1757-899X/580/1/012039.

[30] O.V. Mishin, B. Bay, D. Juul Jensen, Through-thickness texture gradients in cold-rolled aluminum, Metall. Mater. Trans. A Phys. Metall. Mater. Sci. 31 (2000) 1653–1662, https://doi.org/10.1007/s11661-000-0175-2.

[31] O.V. Mishin, E.M. Lauridsen, N.C. Krieger Lassen, G. Brückner, T. Tschentscher, B. Bay, D. Juul Jensen, H.F. Poulsen, Application of high-energy synchrotron radiation for texture studies, J. Appl. Crystallogr. 33 (2000) 364–371, https://doi.org/10.1107/S0021889899016684.

[32] N.D. Stepanov, D.G. Shaysultanov, R.S. Chernichenko, D.M. Ikornikov, V.N. Sanin, S.V. Zherebtsov, Mechanical properties of a new high entropy alloy with a duplex ultra-fine grained structure, Mater. Sci. Eng. A 728 (2018) 54–62, https://doi.org/10.1016/j.msea.2018.04.118.

[33] M. Annasamy, N. Haghdadi, A. Taylor, P. Hodgson, D. Fabijanic, Static recrystallization and grain growth behaviour of Al0.3CoCrFeNi high entropy alloy, Mater. Sci. Eng. A 754 (2019) 282–294, https://doi.org/10.1016/j.msea.2019.03.088.

[34] F. Lin, Y. Zhang, N. Tao, W. Pantleon, D. Juul Jensen, Effects of heterogeneity on recrystallization kinetics of nanocrystalline copper prepared by dynamic plastic deformation, Acta Mater. 72 (2014) 252–261, https://doi.org/10.1016/j.actamat.2014.03.036.

[35] F.J. Humphreys, M. Hatherly, Recrystallization and Related Annealing Phenomena, second ed., Elsevier, 2004 https://doi.org/10.1016/B978-0-08-044164-1.X5000-2.

[36] T. Xiong, S. Zheng, J. Pang, X. Ma, High-strength and high-ductility AlCoCrFeNi 2.1 eutectic high-entropy alloy achieved via precipitation strengthening in a heterogeneous structure, Scr. Mater. 186 (2020) 336–340, https://doi.org/10.1016/j.scriptamat.2020.04.035.

[37] H. Hu, Texture of metals, Texture 1 (1974) 233–258, https://doi.org/10.1155/TSM.1.233.

[38] L.A.I. Kestens, H. Pirgazi, Texture formation in metal alloys with cubic crystal structures, Mater. Sci. Technol. 32 (2016) 1303–1315, https://doi.org/10.1080/02670836.2016.1231746.

[39] S.R. Reddy, S. Yoshida, T. Bhattacharjee, N. Sake, A. Lozinko, S. Guo, P.P. Bhattacharjee, N. Tsuji, Nanostructuring with structural-compositional dual heterogeneities enhances strength-ductility synergy in eutectic high entropy alloy, Sci. Rep. 9 (2019) 11505, https://doi.org/10.1038/s41598-019-47983-y.

[40] N. Tsuji, Y. Ito, Y. Saito, Y. Minamino, Strength and ductility of ultrafine grained aluminum and iron produced by ARB and annealing, Scr. Mater. 47 (2002) 893–899, https://doi.org/10.1016/S1359-6462(02)00282-8.

[41] C.Y. Yu, P.W. Kao, C.P. Chang, Transition of tensile deformation behaviors in ultrafine-grained aluminum, Acta Mater 53 (2005) 4019–4028, https://doi.org/10.1016/j.actamat.2005.05.005.

[42] Y.Z. Tian, S. Gao, L.J. Zhao, S. Lu, R. Pippan, Z.F. Zhang, N. Tsuji, Remarkable transitions of yield behavior and Lüders deformation in pure Cu by changing grain sizes, Scr. Mater. 142 (2018) 88–91, https://doi.org/10.1016/j.scriptamat.2017.08.034.

[43] H. Li, S. Gao, Y. Tomota, S. Ii, N. Tsuji, T. Ohmura, Mechanical response of dislocation interaction with grain boundary in ultrafine-grained interstitial-free steel, Acta Mater 206 (2021) 116621, https://doi.org/10.1016/j.actamat.2021.116621.

[44] F. Otto, A. Dlouhý, Ch. Somsen, H. Bei, G. Eggeler, E.P. George, The influences of temperature and microstructure on the tensile properties of a CoCrFeMnNi high-entropy alloy, Acta Mater 61 (2013) 5743–5755, https://doi.org/10.1016/j.actamat.2013.06.018.

[45] N.D. Stepanov, D.G. Shaysultanov, R.S. Chernichenko, N.Yu. Yurchenko, S.V. Zherebtsov, M.A. Tikhonovsky, G.A. Salishchev, Effect of thermomechanical processing on microstructure and mechanical properties of the carbon-containing CoCrFeNiMn high entropy alloy, J. Alloys Compd. 693 (2017) 394–405, https://doi.org/10.1016/j.jallcom.2016.09.208.

[46] S. Gao, Y. Bai, R. Zheng, Y. Tian, W. Mao, A. Shibata, N. Tsuji, Mechanism of huge Lüders-type deformation in ultrafine grained austenitic stainless steel, Scr. Mater. 159 (2019) 28–32, https://doi.org/10.1016/j.scriptamat.2018.09.007.